Investigation of charge transport mechanism in hydrothermally synthesized reduced graphene oxide (rGO) incorporated zinc oxide (ZnO) nanocomposite films

Nikita Jain[1], Savita Sharma[2], and Nitin K. Puri[1,*]

[1] *Nanomaterials Research Laboratory (NRL), Department of Applied Physics, Delhi Technological University, Delhi 110042, India*
[2] *Physics Department, Kalindi College, University of Delhi, Delhi 110008, India*

ABSTRACT

The present study aims to investigate the impact of reduced graphene oxide (rGO) incorporation on the charge transport properties of zinc oxide (ZnO) nanocomposite films. ZnO and varied weight percentage of rGO (1.25% to 10%) in ZnO-rGO nanocomposites are synthesized via cost-effective and facile hydrothermal method. The effect of varying weight percentage of rGO in ZnO nanocomposite is analysed by techniques such as X-ray diffraction (XRD), Scanning electron microscopy (SEM), Energy dispersive X-ray (EDX), Fourier transform infra-red spectroscopy (FTIR), and Raman spectroscopy. The observed current–voltage (I–V) characteristics at room temperature show the enhancement in forward current with an increasing weight percentage of rGO (1.25% to 10%) in ZnO nanocomposite films. To study the charge transport mechanism in nanocomposite films, dual-logarithmic I–V characteristics are plotted. From the characteristic curves, we find that three different laws of space charge limited conduction (SCLC) model namely Ohm's law, Child's law, and trap-limited SCLC mechanism describe charge transport properties in the ZnO-rGO nanocomposite films. At a low weight percentage of rGO (1.25%) in ZnO-rGO nanocomposite films, a transition from Child's law to trap-limited SCLC mechanism (0.9 V being the cross-over voltage) is obtained. As the weight percentage of rGO in ZnO-rGO nanocomposite films is increased from 2.5 to 10%, the conduction is favored by Ohm's law at low applied voltages to Child's law at higher applied voltages. Best experimental results are shown with 5% of rGO in ZnO-rGO nanocomposite. The prepared nanocomposite films have potential applications in UV-photodetector devices.

Address correspondence to E-mail: nitinkumarpuri@dtu.ac.in

Springer

1 Introduction

Nanocomposites are a blend of dissimilar materials with one or more of their constituents being at the nanoscale range. They offer an opportunity to tailor the properties of material towards a specific application. There has been an enormous interest in nanocomposite materials in recent times, owing to their cost-effectiveness and enhanced properties leading to improved device performance. Hybrid nanocomposites have been developed and explored for profound applications such as photodetectors, supercapacitors, gas sensors, solar cells. [1, 2]. Among the various metal-oxides, zinc oxide (ZnO) is a prominent semi-conductor with a wide range of applications due to its wide-bandgap, large exciton binding energy, abundant availability, non-toxicity, and high photon-absorption [3, 4]. A variety of morphologies can be synthesized by numerous chemical and physical methods widening up the research opportunities towards new technology [4]. Simultaneously, easy tuning of shape, size, and compositions of ZnO play an important role in altering its magnetic, optical, electrical, and other properties for numerous applications [5, 6].

Reduced graphene oxide (rGO), a two-dimensional (2D) material is an expeditious rising star on the horizon of material science and nanotechnology. Its exceptional mobility and conductivity, mechanical flexibility, optical transparency, chemical stability, and high specific surface area is attracting considerable research interest [7]. The sheets of rGO possess a large surface area which may provide support to load other functional nanomaterials. Furthermore, the oxygenated functional groups can act as nucleation centers to support nanomaterials onto graphene sheets which makes it viable to synthesize nanocomposites based on graphene [8].

Various hybrid nanocomposites based on ZnO and rGO have been explored in the field of photodetectors, gas sensors, batteries, supercapacitors, and many more due to their enhanced properties [9–14]. Previously, it has been widely reported about the charge transport properties of ZnO and rGO materials individually and their nanocomposites with other different materials (eg. n-type ZnO grown on plain and focussed ion beam GaN substrates, n-Gallium doped-ZnO on p-Silicon substrate, GaN/rGO nanocomposite with a different weight percentage of

GaN, etc. [15–17]). Soylu et al. studied the effect of the molar concentration of precursors of ZnO on I–V characteristics [18]. Therefore, it is evident that ZnO, rGO, and their nanocomposites with other materials have been explored extensively. However, to the best of our knowledge, no reports are available focussing on a detailed study of the charge transport mechanism in ZnO-rGO nanocomposite films.

A plethora of experimental methods have been rigorously explored for binding of ZnO with rGO such as hydrothermal, aerosol spraying, microwave synthesis, chemical deposition, solvothermal, precipitation methods, and solution combustion synthesis [19–23]. Among these methods, hydrothermal synthesis is considered advantageous as it is cost-effective, uses mild synthesis conditions, and requires low energy with simple equipments resulting in uniform ZnO nanoparticles over rGO nanosheets [24].

In the present work, ZnO and ZnO-rGO nanocomposites with different weight percentage of rGO (from 1.25 to 10%) have been synthesized using hydrothermal method. The charge transport mechanism in the prepared Al/ZnO/ITO and Al/ZnO-rGO/ITO nanocomposite films (rGO varied from 1.25 to 10%) have been studied in detail towards their utilization for UV-photodetector devices.

2 Experimental

2.1 Chemical reagents

The chemicals used in the synthesis are Zinc acetate $(Zn(CH_3COO)_2 \cdot 2H_2O)$, sodium hydroxide pellets (NaOH), graphite powder, concentrated sulphuric acid (H_2SO_4), orthophosphoric acid (H_3PO_4), hydrogen peroxide (H_2O_2), potassium permanganate $(KMnO_4)$, hydrazine hydrate $(N_2H_4 \cdot H_2O)$, and ethanol (C_2H_5OH). All the chemicals are purchased from Fisher Scientific and Sigma Aldrich. All belong to AR grade purity and are employed without further purification.

2.2 Synthesis of ZnO twin-hexapods

Firstly, ZnO twin-hexapods are synthesized using the facile hydrothermal method. In the synthesis, a solution of Zinc acetate (0.2 M) and sodium hydroxide (1.25 M) is prepared separately, with continuous

magnetic stirring for 30 min. Then, the solution of sodium hydroxide is added into zinc acetate solution drop-wise. The pH of the solution is observed to be 6.6. The final solution is kept for stirring for an hour which is then transferred to a 100 ml Teflon-lined steel autoclave, which is heated at 130 °C for 24 h. After several washings with DI and ethanol, the final product is dried overnight.

2.3 Synthesis of rGO

Firstly, GO is synthesized from graphite using improved modified Hummer's method as reported elsewhere [25, 26]. In detail, 2 g of graphite powder is added to a mixture of concentrated sulphuric acid and phosphoric acid in the ratio of 9:1 with continuous stirring. Thereafter, some amount of potassium permanganate is added at a very slow pace to the resulting solution followed by the magnetic stirring of 12 h at 50 °C. After this, the reaction is quenched by adding ice (300 ml) with 2.5 ml of hydrogen peroxide solution. Finally, the yellowish slurry mixture is washed (until the pH reached to 7), filtered, and dried to obtain the final product. For the synthesis of rGO, 200 mg of GO powder so obtained is dispersed in 200 ml of DI water and ultrasonicated for an hour. Then it is transferred onto the stirrer and 100 µL of hydrazine hydrate is added drop-wise into it which acts as a reducing agent and the solution is left for 12 h stirring at a particular temperature. The final solution turns black which then is washed, filtered, and dried to obtain rGO.

2.4 Synthesis of ZnO-rGO nanocomposites

Various nanocomposites of ZnO-rGO are synthesized via hydrothermal route by varying weight percentage of rGO (from 1.25 to 10%) in ZnO. Typically, a suitable amount of rGO (1 mg/ml) is dispersed in ethanol with ultrasonic treatment for an hour. Meanwhile, a solution of Zinc acetate (0.2 M) and sodium hydroxide (1.25 M) is prepared separately with stirring. It is followed by mixing of all three resulting solutions under continuous stirring for an hour. The observed pH of the solution (ZnO-rGO nanocomposite) is 6.6. At last, the solution is transferred to a Teflon-lined stainless-steel autoclave which is heated at 130 °C for 24 h. After several washings with DI water and ethanol, the grey color powder is obtained which is then dried overnight.

Weight percent variation by volume (w/v) of 1.25%, 2.5%, 5%, and 10% of rGO to ZnO are prepared and named as ZG-1.25, ZG-2.5, ZG-5, and ZG-10, respectively. All these ZnO-rGO nanocomposites with various rGO content are prepared by above said process.
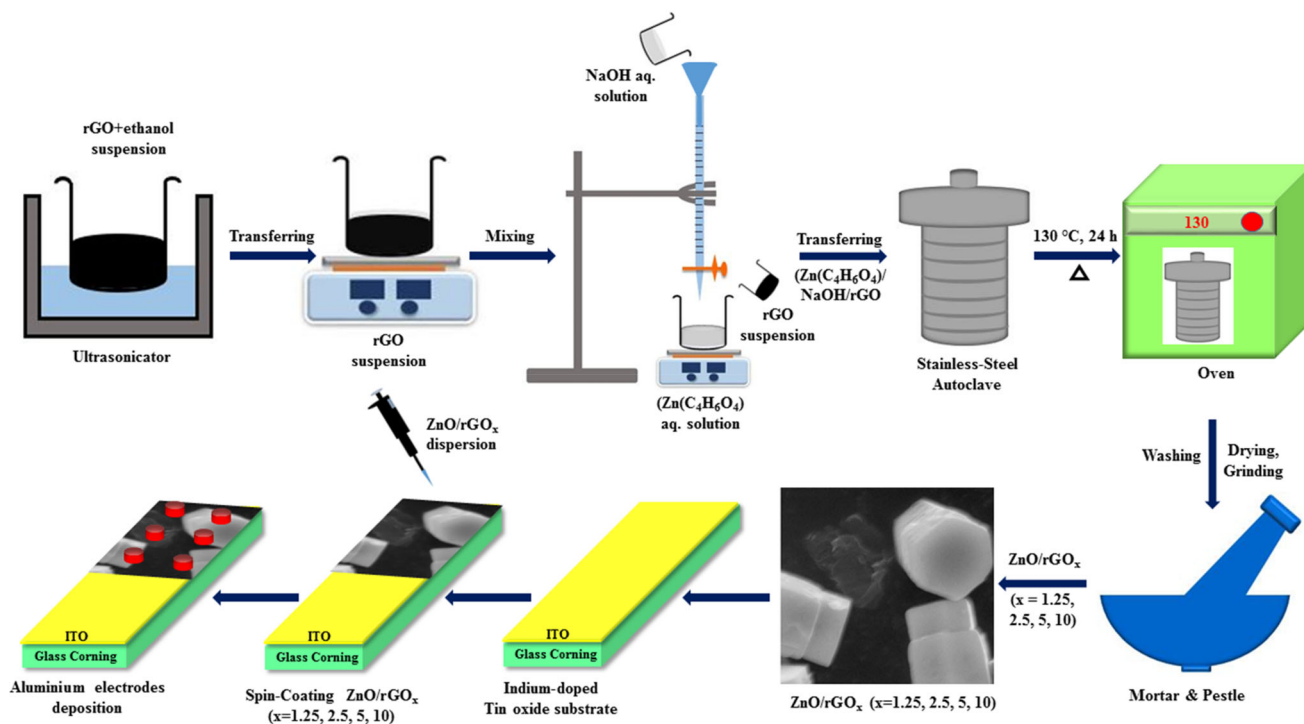
2.5 Film fabrication

ZnO-rGO nanocomposite films are fabricated on rectangular indium tin-oxide (ITO) coated corning-glass substrates. The standard wet cleaning method is employed to clean the ITO substrates. Briefly, soap solution, deionized ionized (DI) water, acetone, and finally with isopropyl alcohol. After cleaning, the substrates are dried at 100 °C on a hot plate for 30 min. In the first step, ZnO powder is dispersed in ethanol by ultrasonicating it for 30 min. In the second step, ZnO films are prepared via spin-coating technique, by dispensing the above solution on ITO substrates at 3000 rpm for 60 s. It is followed by drying the films in the open air at 70 °C for 10 min. A similar process is devised to obtain all the desired ZG-1.25, ZG-2.5, ZG-5, and ZG-10 nanocomposites films. Finally, 100 nm thick top Al metal electrodes are deposited on the prepared films using the thermal evaporation technique. Figure 1 shows the schematic description of the process of fabrication of Al/ZnO-rGO/ITO nanocomposites films.

3 Results and discussions

All the prepared samples are thoroughly characterized using various techniques such as X-ray diffraction (XRD), Scanning electron microscopy (SEM), Energy dispersive x-ray (EDX), Fourier transform infra-red spectroscopy (FTIR), and Raman spectroscopy. Charge transport properties of all the prepared films (Al/ZnO/ITO, Al/ZnO-rGO/ITO) have been studied via current–voltage (I–V) characteristics over the voltage range of − 2.5 to 2.5 V using Keithley 2450 SMU.

3.1 Structural analysis (X-ray diffraction)

The XRD pattern of ZnO, ZG-1.25, ZG-2.5, ZG-5, and ZG-10 nanocomposite is shown in Fig. 2. XRD pattern of ZnO shows all the diffraction peaks which are congruous with the standard data available for the

Fig. 1 Schematic description of fabrication of Al/ZnO-rGO/ITO nanocomposites films

Fig. 2 XRD pattern of ZnO, ZG-1.25, ZG-2.5, ZG-5, and ZG-10 nanocomposites
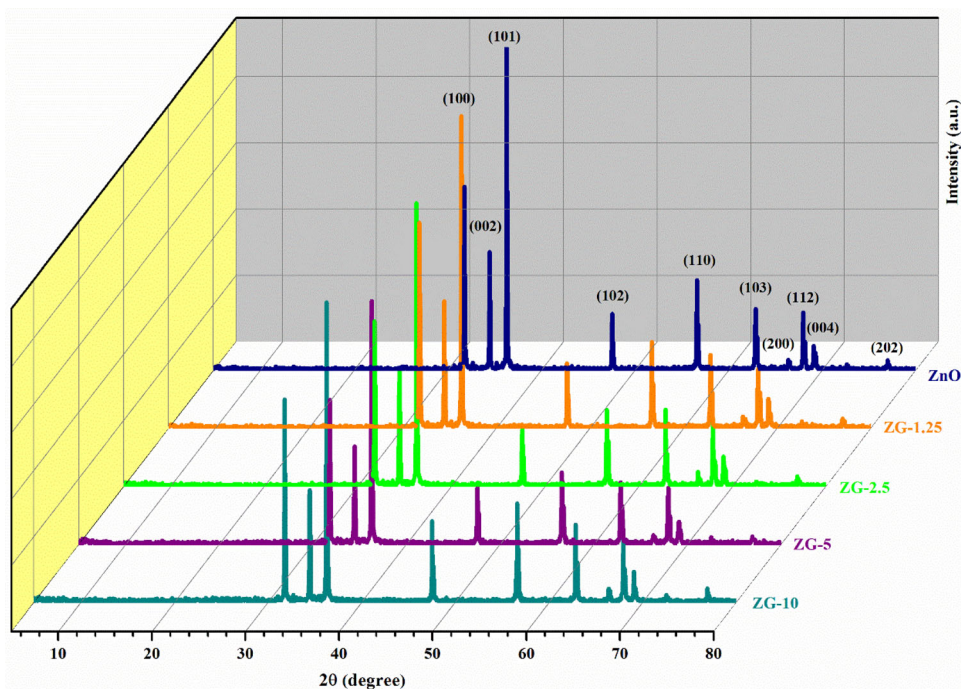
wurtzite structure of ZnO (JCPDS 36-1451) [27]. A prominent diffraction peak of GO (Fig. S1a in the Supplementary Information) is found to be at 11.7° and a weak peak located at 42.6° corresponding to (002) and (100) reflection, respectively. The inset of

Fig. S1a in the Supplementary Information shows the diffraction pattern of raw graphite which shows a highly crystalline and strong diffraction peak at 26.6° towards the (002) plane. The shift in GO peak at a lower diffraction angle confirms the successful

oxidation of graphite [28]. The broadening and shifting of the distinct peak of GO from 11.7° to 23.1° can be attributed to the breakdown of the long-range order of GO [29]. Two broad diffraction peaks located at 23.1° and 43.6° correspond to rGO (Fig. S1b in the Supplementary Information). These two peaks confirm the formation of (002) and (100) planes of rGO [29]. The peak positions of ZnO remain the same in all ZnO-rGO nanocomposites (Fig. 2) while the two reflection peaks of rGO are absent in nanocomposites. The reason can be attributed to the low diffraction intensity of rGO in the dispersed state [30, 31].

The d-spacing of graphite, GO and rGO is calculated using Bragg's relation [32] and is found to be 0.33 nm, 0.75 nm, and 0.38 nm, respectively for the (002) plane. The increase of d-spacing of GO compared to graphite can be due to the intercalation of oxygenated functional groups (such as epoxide and hydroxyl groups) and intercalation of molecules of water in the interlayer spacing of carbon layers [28].

The average crystallite size of ZnO and ZnO-rGO nanocomposites is calculated using Scherrer's relation [33, 34]. The crystallite size calculated for ZnO, ZG-1.25, ZG-2.5, ZG-5, and ZG-10 samples is 81, 77, 76, 70, and 74 nm, respectively. It is observed that the crystallite size of ZnO decreases progressively as the weight percentage of rGO in the nanocomposites is increased to 5%. This suggests that the growth and nucleation stage of ZnO crystals in the nanocomposites is hindered by rGO [4]. Furthermore, the dislocation density (δ) of ZnO and ZnO-rGO nanocomposite is calculated using the following relation: $\delta = 1/D^2$ where D is the crystallite size of ZnO and ZnO-rGO nanocomposite. The highest and lowest dislocation density is found to be approximately 2.05×10^{-4} nm^{-2} and 1.49×10^{-4} nm^{-2} for ZG-5 nanocomposite and ZnO, respectively. When the dislocation density decreases, the crystallinity increases [35]. The intensity of the diffraction peak along the (101) diffraction plane is supporting this phenomenon. The diffraction peaks of the composite ZG-1.25 are stronger than those of other nanocomposites but weaker than the diffraction peak of pure ZnO which indicates that the crystallinity of the composite is affected by the addition of rGO [20].

The lattice parameters (lattice constants and volume of unit cell) are calculated by means of Rietveld refinement using FullProf Software. Best matching of the peaks for all the samples is observed for hexagonal structure with P6$_3$mc space group. Table 1

shows the calculated values of FWHM, lattice parameters, crystallite size, and dislocation density for all the prepared samples. It is clear from the table that the structural lattice parameters increases and the crystallite size decreases with the increasing weight percentage of rGO in the ZnO-rGO nanocomposites upto 5%. The obtained results are consistent with the literature [36–38].

On the other hand, the variation in the trend of certain crystal parameters of ZG-10 nanocomposite can be understood as: at this concentration, the ratio of zinc ions to rGO is not critical. Since the critical ratio is not maintained, the sorption of zinc ions is less on rGO nanosheets, due to which the synergetic effect could not follow the trend as followed by the other nanocomposites.

3.2 SEM and EDX observations

SEM analysis is done to investigate the surface morphology as well as to examine the average length of the prepared twin-hexapods of ZnO, ZG-1.25, ZG-2.5, ZG-5, and ZG-10 nanocomposites. Figure 3 shows the SEM images of the prepared ZnO and ZnO-rGO nanocomposite with variation in weight percentage of rGO from 1.25 to 10%. It is observed that the average length of the hexapods is closely related to the weight percentage of rGO in the ZnO-rGO nanocomposite. Figure 3a depicts the SEM image of ZnO. The observed average length of the top-hexapod is 2.7 μm and the average length of the bottom-hexapod is 5 μm. Compared to the crystallite size of the samples calculated by the XRD analysis, a bigger particle size of ZnO and ZnO-rGO nanocomposites (rGO varied from 1.25 to 10%) is obtained from SEM observations. This can be due to the fact that particles contain many smaller crystallites [39, 40]. When rGO is introduced in the ZnO framework, the morphology is maintained as can be seen (Fig. 3b–e). The top-hexapod of the ZG-1.25 nanocomposite (Fig. 3b) has an average length of 1.7 μm and the average length of the bottom-hexapod is 3.1 μm. Thus, we can clearly see that the size of ZnO hexapods decreases with the increase in the concentration of rGO in nanocomposites. Top-hexapods of average length 1.6 μm and bottom-hexapod of the average length of 2.9 μm is obtained when the rGO concentration is increased to 2.5% in ZnO (Fig. 3c). But, further increase in rGO concentration to 5% in ZnO-rGO nanocomposite the ZnO twin-hexapods are found to be comparatively

Table 1 Variation in FWHM, lattice parameters (lattice constants and volume of unit cell), crystallite size and dislocation density of (a) ZnO, (b) ZG-1.25, (c) ZG-2.5, (d) ZG-5, and (e) ZG-10 nanocomposites with variation in weight percentage of rGO

Sample	Plane	2θ (degree)	FWHM (degree)	Lattice parameters		Volume of unit cell (Å^3)	Crystallite size (nm)	Dislocation density (nm^{-2}) $\times 10^{-4}$
				a (Å)	c (Å)			
ZnO	(101)	36.3	0.10	3.2465	5.2021	47.48	81	1.49
ZG-1.25	(101)	36.3	0.10	3.2477	5.2034	47.53	77	1.67
ZG-2.5	(101)	36.3	0.11	3.2481	5.2040	47.54	76	1.74
ZG-5	(101)	36.3	0.11	3.2485	5.2041	47.55	70	2.05
ZG-10	(101)	36.3	0.11	3.2480	5.2039	47.54	74	1.82

small with an average length of 1.2 μm and 2.4 μm (Fig. 3d) of top and bottom-hexapod, respectively. The reason is the formation of rGO sheets which creates a hindrance for further growth of ZnO hexapods which is consistent with the XRD analysis as well.

On the other hand, when the rGO concentration is increased to 10% in ZnO-rGO nanocomposite, most of the rGO sheets in the nanocomposite are agglomerated and some of the ZnO grow on graphene sheets. To understand and deduce the ongoing observation in surface morphology, the formation process of ZnO-rGO nanocomposite is surmised. There should be a critical ratio of zinc ions of ZnO and rGO to form well-dispersed nanocomposites. When the concentration of rGO is low, the ratio of zinc ions is relatively high in rGO. This leads to excess sorption of zinc ions on rGO sheets which results in well-dispersed ZnO-rGO nanocomposite. On increasing the concentration of rGO in ZnO, the sorption of zinc ions is less on rGO sheets. The negative charges on reduced graphene oxide are partially neutralized by the zinc ions. This lead to the coagulation of rGO sheets during the reaction process [41]. It is observed that the top-hexapod of ZnO in this nanocomposite has an average length of 1.5 μm and the bottom-hexapod has an average length of 2.7 μm (Fig. 3e). But, an increase in rGO concentration in the nanocomposites does not result in the agglomeration of ZnO hexapods. From the above observation, we can deduce that rGO nanosheets co-exist with the ZnO twin-hexapods in the fabricated ZnO-rGO nanocomposites.

The elemental composition of ZnO and ZnO-rGO nanocomposites are analysed by the EDX spectrum.

It is inapt to determine the exact content of the elements present in the ZnO and ZnO-rGO nanocomposites using EDX because of the presence of light elements (O and C) [42]. EDX spectra and the weight percent composition of ZnO and ZnO-rGO nanocomposites are shown in Fig. S2 in Supplementary Information. As can be seen from the EDX spectra of ZnO (S2a in Supplementary Information), no peak corresponding to carbon is found. With the addition of rGO in the ZnO framework, increasing weight percent of carbon peak is observed in all the ZnO-rGO nanocomposites (Fig. S2b–e in Supplementary Information). However, an impurity peak of sodium is also found in all the samples. This impurity peak could be due to the precursor (NaOH) used in the synthesis of ZnO and ZnO-rGO nanocomposites. Although its weight percent composition is negligibly small, yet it may be one of the reasons for the creation of traps inside ZnO and ZnO-rGO nanocomposite [43].

3.3 FTIR Spectroscopy analysis

FTIR Spectroscopy is performed to investigate and elucidate the presence of functional groups related to ZnO, GO, rGO along with the other functional groups which may arise after hybridization in prepared samples. Figure 4 shows the FTIR spectra of ZnO, ZG-1.25, ZG-2.5, ZG-5, and ZG-10 nanocomposites. The spectrum of ZnO (Fig. 4a) exhibits a broad peak at 3278 cm^{-1} which corresponds to O–H stretching vibrations [44]. Few narrow peaks 2830 to 2955 cm^{-1} correspond to C–H bonds [45]. Several peaks appearing between 1360 and 1710 cm^{-1} can be attributed to the stretching modes of COOH group, which are believed to be adsorbed on the surface of
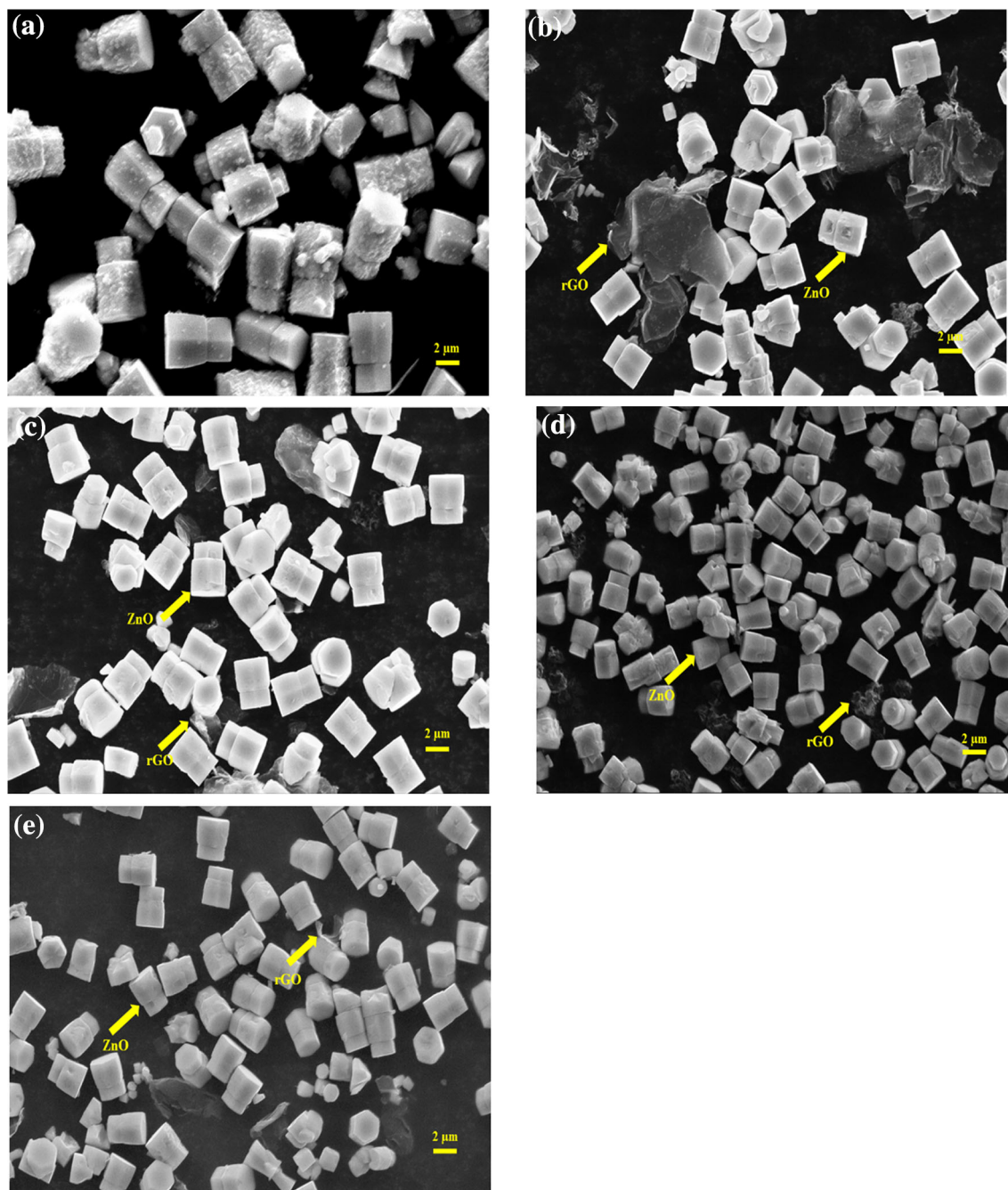
Fig. 3 SEM images of ZnO and ZnO-rGO nanocomposites: **a** ZnO, **b** ZG-1.25, **c** ZG-2.5, **d** ZG-5, and **e** ZG-10

the ZnO hexapods during the process of synthesis [46]. In addition to this, a small peak at 920 cm^{-1} and a pointed peak at 457 cm^{-1} corresponds to Zn–O stretching and deformation vibrations, respectively [46, 47]. FTIR spectrum of GO (Fig. S3a in the Supplementary Information) consists of broad peak 3290 cm^{-1} corresponding to O–H groups and narrow peaks at 2868 cm^{-1} corresponding to C–H stretching. In addition to this, the peak at 1705 cm^{-1} and

1577 cm^{-1} corresponds to C=O and C=C stretching. A small peak at 1395 cm^{-1} corresponds to O–H deformation. Finally, two peaks at 1230 and 1056 cm^{-1} confirm the epoxy C–O–C and alkoxy C–O stretching vibrations, respectively [48]. When GO is reduced to rGO using hydrazine hydrate, the oxygen-containing functional groups are significantly reduced and weakened which is clear in the FTIR spectrum of rGO (Fig. S3b in the Supplementary
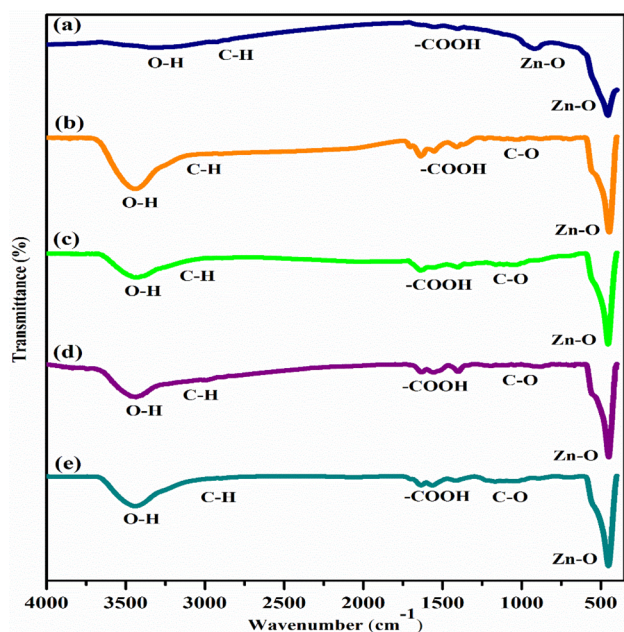
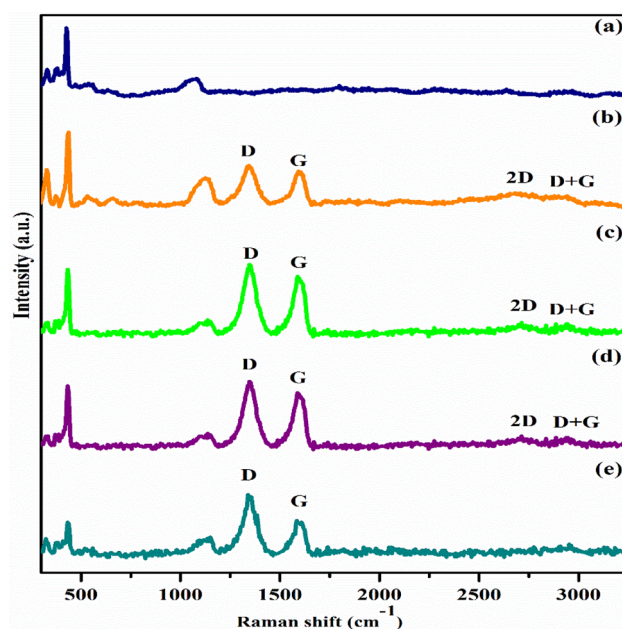**Fig. 4** FTIR spectra of ZnO and ZnO-rGO nanocomposites: a ZnO, b ZG-1.25, c ZG-2.5, d ZG-5, and e ZG-10

Information). The peak at 3450 cm^{-1} is attributed to O–H group. The two new peaks at 1640 cm^{-1} and 1369 cm^{-1} arise due to the cyclic hexagonal symmetry and the vibrations of skeletal of rGO, respectively [47]. Two peaks at 1230 and 1056 cm^{-1} confirm the epoxy C–O–C and alkoxy C–O stretching vibrations, respectively which are also present in GO. The FTIR spectrum of ZnO-rGO nanocomposites (Fig. 4b – e) contains a broad absorption band at 3440 cm^{-1} denoting the O–H groups and a few tiny peaks around 2900 cm^{-1} confirming C-H bonds. Various peaks in the range of 1350 to 1600 cm^{-1} are due to the stretching modes of the COOH group. Furthermore, few weak peaks around 1100 cm^{-1} are attributed to C–O stretching vibrations of rGO sheets. A peak around 457 cm^{-1} is the characteristic peak of ZnO and corresponds to the Zn–O bond confirms the presence of ZnO in all the nanocomposites [9, 21]. Hence, this indicates the coexistence of ZnO and rGO phase in all the prepared ZnO-rGO nanocomposites which is in good accordance with the SEM observations as well.

3.4 Raman Spectroscopy analysis

The Raman spectra of ZnO, GO, rGO and ZG-1.25, ZG-2.5, ZG-5, and ZG-10 nanocomposites is shown in Fig. 5 and the detailed parameters are calculated

from Raman data are summarized in Table 2. Raman spectroscopy measurements of ZnO (Fig. 5a) show peaks at 332, 387, 437, 559, and 1145 cm^{-1}. The peak with Raman shift of 332 cm^{-1} corresponds to acoustic and optical phonon overtone with A_1 symmetry while the peak located at 387 cm^{-1} corresponds to A_1(TO) mode [30]. The peak at 437 cm^{-1} corresponds to the ZnO non-polar optical phonons (E_{2high}). It signifies the crystal quality and is the characteristic peak of hexagonal wurtzite phase of ZnO [49]. A peak at 559 cm^{-1} confirms the A_1(LO) mode which is attributed to the surface defect formation of ZnO [50]. A spectral peak at 1145 cm^{-1} is attributed to the multi-phonons process [51].

Two characteristic peaks of GO are observed at 1352 cm^{-1} and 1600 cm^{-1} which corresponds to the D and G bands of graphene, respectively (Fig. S4a in the Supplementary Information). The D band represents lattice disorders in the sp^2-hybridized C atoms and the G band is related to the highly oriented sp^2 hexagonal graphitic lattice [52]. Structural changes from GO to rGO upon chemical reduction are reflected in the spectrum clearly (Fig. S4b in the Supplementary Information). The D and G bands of rGO are located at 1347 cm^{-1} and 1575 cm^{-1}, respectively. The intensity ratio (I_D/I_G) increased from 0.99 to 1.07 when GO is chemically reduced to rGO indicating the partial modification of surface

Fig. 5 Raman spectra of ZnO and ZnO-rGO nanocomposites: a ZnO, b ZG-1.25, c ZG-2.5, d ZG-5, and e ZG-10

Table 2 Parameters calculated from Raman data of (a) GO, (b) rGO, (c) ZG-1.25, (d) ZG-2.5, (e) ZG-5, and (f) ZG-10 nanocomposites

Sample	Position of D band/cm^{-1}	Position of G band/cm^{-1}	I_D/I_G	FWHM (cm^{-1})	
				D-band	G-band
GO	1352	1600	0.99	102	66
rGO	1347	1575	1.07	85	65
ZG-1.25	1343	1591	1.01	88	66
ZG-2.5	1347	1587	1.01	83	66
ZG-5	1351	1579	1.01	81	66
ZG-10	1339	1583	1.01	86	67

functional groups containing oxygen [52]. The results indicate that GO is successfully reduced to rGO after chemical reduction by hydrazine hydrate.

The Raman spectrum of all the prepared nanocomposites (Fig. 5b – e) contains the Raman bands of ZnO and rGO which confirms that the nanocomposites are successfully synthesized [53]. The I_D/I_G ratio of all the ZnO-rGO nanocomposites decreases to 1.01 compared to rGO which indicates that the sp^2 domain size of carbon atoms decreases with the incorporation of rGO in ZnO [10]. The D band shifts from 1343 to 1351 cm^{-1} and the G band decreases from 1591 to 1579 cm^{-1} as the weight percentage of rGO increases from 1.25 to 5% in ZnO. But, the same trend of shifting in the D and G band is not observed in ZG-10 nanocomposite.

A small shifting in the D and G band (Table 2) of the Raman spectrum of the nanocomposites is attributed to the electronic interactions of ZnO and rGO during the hydrothermal synthesis process [49]. In the nanocomposites, the 2D band is at ~ 2700 cm^{-1} and the D + G band is at ~ 2900 cm^{-1} which reconfirms the presence of rGO in the nanocomposites. The 2D and D + G bands of ZG-10 nanocomposite are not observed clearly.

To derive more quantitative information, the Raman spectra of GO (Fig. S4a in the Supplementary Information), rGO (Fig. S4b in the Supplementary Information), ZnO and ZnO-rGO nanocomposites is further deconvoluted (Fig. 6). The full-width half maximum (FWHM) is calculated using deconvoluted D and G bands (Table 2). It is found that when GO is reduced to rGO the FWHM values for both the bands decreases. The decrease in the width of the D-band of rGO is attributed to an increase in carbon-sp^2 content [54]. The lower the value of the width of G-band of rGO, higher its degree of crystallization [55]. Furthermore, with the addition of rGO (from 1.25 to 5%) in the ZnO-rGO nanocomposite, the width of the
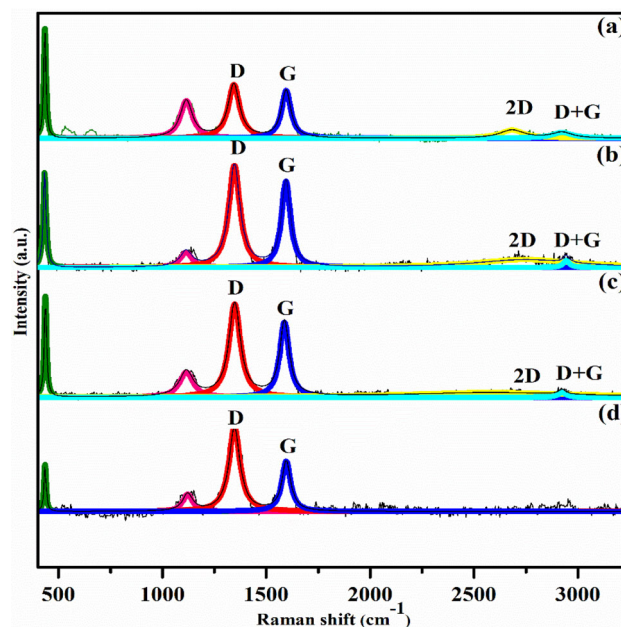
Fig. 6 The deconvoluted Raman data of ZnO and ZnO-rGO nanocomposites: a ZnO, b ZG-1.25, c ZG-2.5, d ZG-5, and e ZG-10

D-band first increases and then decreases as compared to rGO. Consequently, the carbon-sp^2 content of the ZG-5 nanocomposite is more than the ZG-1.25 nanocomposite. The width of the G-band remains almost the same in all the prepared nanocomposites. This indicates that the crystallization of rGO is maintained in all the nanocomposites. For ZG-10 nanocomposite, the width of D and G bands deviates from the trend as followed by all the other nanocomposites.

The reason for the deviation from the trend in Raman results of ZG-10 nanocomposite can be inferred as: The uncritical ratio of zinc ions to rGO does not lead to the synergetic effect between ZnO and rGO. Because of this, the ZG-10 nanocomposite cannot follow the trend as followed by the other

nanocomposites. The co-observed Raman peaks of ZnO together with rGO confirm that the ZnO-rGO nanocomposites are synthesized successfully which is in good accordance with the SEM and FTIR Spectroscopy results as well.

3.5 Electrical analysis of films

The impact of incorporation rGO on electrical properties [56, 57] of ZnO is studied using room temperature I–V plots using Keithley 2450 SMU. Figure 7 shows the illustration of I–V measurement experimental setup. Figure 8 represents the current–voltage (I–V) characteristics for Al/ZnO/ITO and Al/ZnO-rGO/ITO films with variation in weight percentage of rGO in ZnO. Figure 9a–e shows the variation in dual-logarithmic I–V curves with a varying weight percentage of rGO from 1.25 to 10% in the prepared nanocomposite films.

As can be seen from the I–V curves (Fig. 8), the forward current in the ZnO films is 51 μA at 2.5 V. When the weight percentage of rGO is increased from 1.25 to 10% in ZnO nanocomposite films (as confirmed from the EDX spectra), the forward current is found to be increasing from ≈ 51 to 105 μA (Table S1 in Supplementary Information). When rGO is incorporated from 1.25 to 5% in ZnO nanocomposite films, the leakage current under applied reverse bias voltage is found to be decreasing from 71 to 35 μA at 2.5 V. It is also found that the forward and reverse voltage in ZG-10 nanocomposite films could reach a maximum of 1.75 V after which the films breakdown. The enhancement in forward current and reduction in leakage current in the prepared nanocomposite films can be attributed to rGO nanosheets which provided a facile pathway for the direct transportation of charge carrier in the ZnO-rGO nanocomposite [58]. SEM and EDX observations, FTIR, and RAMAN
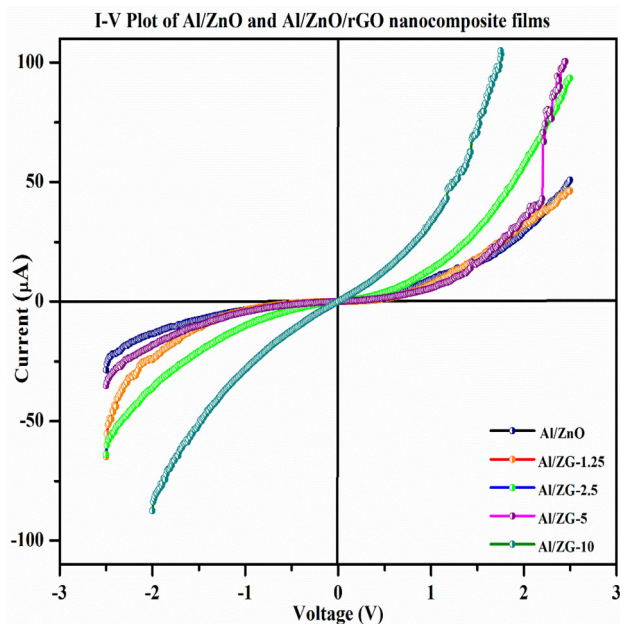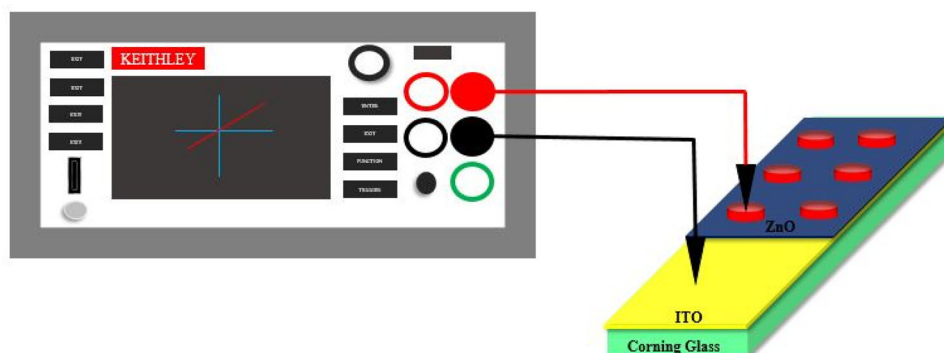
Fig. 8 Current–Voltage characteristics of ZnO and ZnO-rGO nanocomposite films

Spectroscopy analysis support these results by showcasing the coexistence of ZnO and rGO in all the prepared ZnO-rGO nanocomposites. When an external bias is applied to the films, mobility as well as the drift velocity of the charge carriers increases which thereby increased the forward current. The increase in leakage current in the ZG-10 nanocomposite films can be ascribed to the formation of trap-level defects in ZnO due to the high concentration of rGO.

The rectification ratio (RR = I_F/I_R) is calculated for all the film samples [59]. In this case, the RR is calculated as: the forward current at 2.5 V divided by the reverse current at -2.5 V for all the films except for ZG-10 nanocomposite films. The RR for ZG-10 nanocomposite films is calculated as: the forward

Fig. 7 Illustration of I–V measurement experimental setup
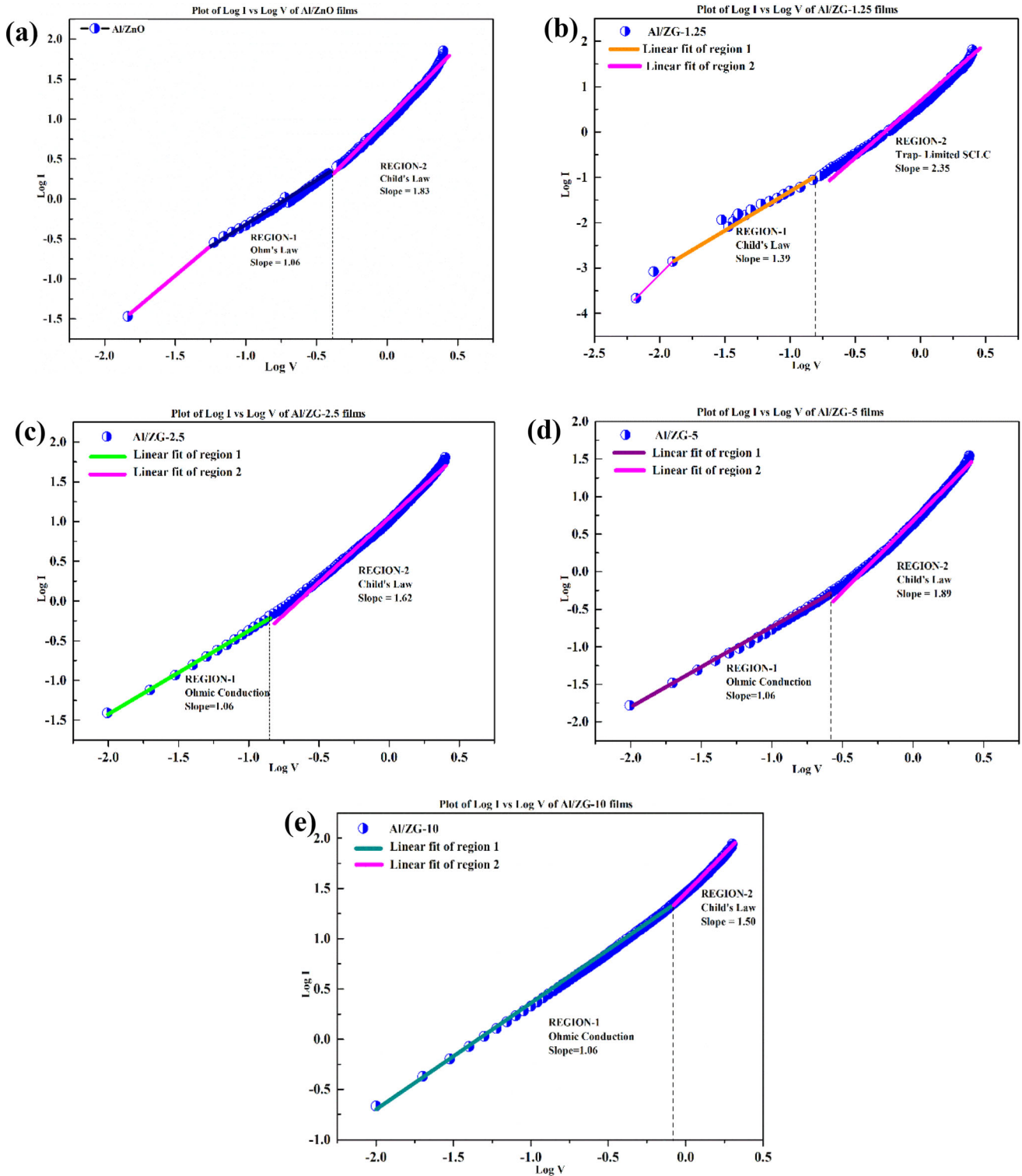
Fig. 9 Dual-logarithmic I–V curves obtained for **a** ZnO, **b** ZG-1.25, **c** ZG-2.5, **d** ZG-5, and **e** ZG-10 nanocomposite films with standard error $\leq \pm 0.002$

current at 1.75 V divided by the reverse current at − 1.75 V. The RR is found to be 0.7, 1.2, 1.5, 2.9, and 1.6 for Al/ZnO, Al/ZG-1.25, Al/ZG-2.5, Al/ZG-5, and Al/ZG-10 nanocomposite films, respectively.

The I–V curves of all the samples are almost symmetric in the forward and reverse direction, which results in low RR of Al/ZnO and Al/ZnO-rGO nanocomposite films. The reason can be attributed to the low work function contrast between the ZnO and Al electrodes, ZnO-rGO nanocomposite, and Al electrodes [60]. Table S1 in the Supplementary Information depicts the variation in electrical parameters of the fabricated ZnO and ZnO-rGO nanocomposite films with varying weight percentage of rGO from 1.25 to 10%.

To understand the effect of weight percentage variation of rGO in ZnO nanocomposite films on underlying current conduction mechanism, linear fittings of the obtained I–V curves are carried out. All the I–V curves are fitted by the space charge limited conduction (SCLC) mechanisms, which is similar to the results reported in the literature [18, 43, 61, 62]. The standard error for linear fitting of different regions in the current–voltage curves is found to be $\leq \pm 0.002$. The relationship between the current generated and applied voltages can be directly interpreted from the value of the obtained slopes from dual-logarithmic I–V curves. The obtained slopes imply that the charge transport mechanism in prepared ZnO-rGO nanocomposite films is governed by the three limiting laws of space charge limited conduction (SCLC) model, which are Ohm's law, Child's law, and trap-limited SCLC mechanism. The power-law relationship ($I \propto (V)^m$, where m is the slope of the plots) is used to categorize the charge transport mechanism in all the films [43]. Such a mechanism is explained based on deep-level defects. Traps capture the electronic charges, which generally lie in the forbidden gap region or extended band tails. Energetically favored states or trap states strongly influence the conduction characteristics in semiconducting materials. The reason for the creation of traps could be (1) inadvertent impurities, (2) defects introduced during the film processing [63–66]. Moreover, the addition of rGO with different weight percentage in ZnO nanocomposite films could also be the cause of interfacial defect states in the prepared films which is supported by the XRD analysis as well. The XRD analysis clearly shows an increase in dislocation density, variation in lattice parameters, and decrease in crystallite size of ZnO with the increase in weight percentage of rGO in ZnO-rGO nanocomposites. Further, EDX spectra show the presence of sodium in the as-synthesized samples which may also be one of the reasons for the creation of traps inside ZnO and ZnO-rGO nanocomposite.

Figure 9a depicts the dual-logarithmic I–V curve of ZnO films. It is observed that for low applied voltages i.e., for $V \leq 0.9$ V (Region-1), the slope of the dual-logarithmic I–V plots comes nearly one. This implies linear dependence of current on the applied voltage. Hence, it is concluded that the conduction mechanism is governed by Ohm's law. Such behavior is because the density of thermally generated free carriers inside the ZnO films is more than those of the injected charge carriers [42]. The weak injection of charge carriers from the electrodes leads to the partial filling of the trap centers. Again to maintain the neutrality of the charges inside the films, redistribution of the charge carriers occurs. This redistribution occurs in such a manner that the injected carriers are still obstructed to travel across the films which results in a slope of 1.06. At higher applied voltage (V ≥ 0.9 V), the departure from ohmic behavior is observed thereby following the Child's Law. This is denoted by Region-2, where the electrons injected from the electrodes to the films are high. Due to which the accumulation of the charge carriers at the electrodes forms a space charge region which thereby affects the electrical distribution.

Figure 9b shows the log$I$—log$V$ curves of ZG-1.25 nanocomposite films. When rGO is introduced in the ZnO nanocomposite films, the charge carriers are increased. These charge carriers facilitate the injected charge carriers upto a certain limit to travel across the prepared films. But the effect due to traps overshadows the carriers of rGO and results in a slope of 1.39 at a low applied voltage (V ≤ 0.9 V) indicating Child's law SCLC mechanism. A transition from Child's Law to trap-limited SCLC mechanism is observed at a higher applied voltage (V ≥ 0.9 V). The strong injection of charge carriers at higher applied voltage occurs, due to which the carriers do not get enough transit time for reapportioning via thermally generated charge carriers or rGO charge carriers. This leads to the filling of trap centers. Hence, a slope greater than 2 is obtained which confirms the trap-limited SCLC conduction mechanism.

Figure 9c–e depicts the dual-logarithmic I–V curves of ZG-2.5, ZG-5, and ZG-10 nanocomposite films. It is observed that as the concentration of rGO is increased from 2.5 to 10% in the ZnO nanocomposite films, a clear transition of the voltage ranges for ohmic conduction keeps on increasing thereby

decreasing the voltage range for Child's Law mechanism. Apart from the prepared ZG-1.25 nanocomposite films, in which the transported charge carriers are low in comparison to the other nanocomposite films with high rGO content, all the nanocomposite films followed the same trend. The reason for such a behavior is explained based on deep-level defects as: It can be observed that for low applied voltages i.e., (Region-1), the slope of the plots comes nearly one. The films are said to follow Ohm's law. The charge carriers due to rGO incorporation increases, which not only facilitates the injected charge carriers to travel across the films but also overshadows the effect of traps. As the voltage increases, the prepared films follow Child's Law. This implies that the strong injection of charge carriers occurs due to which accumulation of the charge carriers at the electrodes form a space charge region which thereby affects the electrical distribution. Hence, the dual-logarithmic I–V characteristics of the prepared ZnO and ZnO-rGO nanocomposite films are dominated by the SCLC conduction mechanism.

4 Conclusion

Motivated by the adjoining merits of ZnO and rGO, the present study addresses the fundamental charge transport properties of ZnO and ZnO-rGO nanocomposite films and their potency for the realization of film-based nanodevices. The nanocomposites are synthesized by a facile hydrothermal method and are analysed by various characterizations. Phase formation of ZnO and dispersion of rGO in ZnO are confirmed by XRD and SEM observations. The elemental composition of ZnO and ZnO-rGO nanocomposites is confirmed by EDX analysis. The coexistence of ZnO and rGO in the nanocomposites is confirmed by FTIR and Raman spectroscopy. Films of ZnO and the ZnO-rGO nanocomposites are fabricated on ITO coated corning-glass substrate using spin-coating technique. Charge transport properties of all the as-prepared films (Al/ZnO/ITO and Al/ZnO-rGO/ITO) have been studied via current–voltage (I–V) characteristics over the voltage range of − 2.5 to 2.5 V. The detailed I–V curves shows the enhancement in the performance characteristics of the nanocomposites films by varying the rGO concentration in ZnO-rGO nanocomposite. It is found that as the rGO concentration increases in ZnO

nanocomposite films, the forward current in the films also increases. Furthermore, the dual-logarithmic I–V plots have been explained based on the space charge limited conduction (SCLC) model to identify the charge transport mechanism in the films. As the weight percentage of 1.25% of rGO is introduced in ZnO nanocomposite films, the dual-logarithmic I–V characteristics give a clear transition from Child's law to trap-limited SCLC mechanism (0.9 V being the cross-over voltage). On further incorporation of rGO (from 2.5 to 10%), the conduction is favored by Ohm's law at low applied voltages and Child's law at higher applied voltages. Experimental results show that the best percentage of rGO in ZnO-rGO nanocomposite films is 5% in respect of high forward current, low leakage current, and higher rectification ratio compared to other ZnO-rGO nanocomposites. Beyond 5% of rGO in ZnO-rGO nanocomposites, the critical ratio of zinc ions to rGO is not maintained, due to which the synergetic effect did not lead to expected results. Hence, manipulation of functional properties such as charge transport by the addition of highly conducting rGO may provide additional liberty during device fabrication suitable for applications such as UV-photodetection.

Declarations

Conflict of interest The authors declare that there is no conflict of interest.

Supplementary Information: The online version contains supplementary material available at https://doi.org/10.1007/s10854-021-07445-6.

References

1. R. Ramírez-Amador, J. Alvarado, G. Flores-Carrasco, L. Morales-Delagarza, S. Alcántara-Iniesta, A. Luna-Flores, Y.P. Bernal, M.Á. Méndezrojas, J.J. Gervacio-Arciniega, H.P. Martínez Hernández, J.F. Curioca-Vega, The influence of deposition time on the structural, morphological, optical and electrical properties of ZnO-rGO nanocomposite thin films grown in a single step by USP. Curr. Comput.-Aided Drug Des. **10**(2), 73 (2020). https://doi.org/10.3390/cryst10020073

2. I. Sameera, R. Bhatia, V. Prasad, R.J.A.P.L. Menon, Temperature dependent current-voltage characteristics of zinc oxide nanowire/polypyrrole nanocomposite. Appl. Phys. Lett. **105**(23), 232112 (2014). https://doi.org/10.1063/1.4903923

3. Liyana, G.R., Sofyan, N., Dhaneswara, D., Subhan, A., Yuwono, A.H.: Optoelectronic properties of ZnO nanorods thin films derived from chemical bath deposition with different growth times. In: AIP Conference Proceedings, vol. 1, p. 030008. AIP Publishing LLC. (2020) https://doi.org/10.1063/5.0015869

4. D. Nath, S. Mandal, D. Deb, J. Rakshit, P. Dey, J.J.J.O.A.P. Roy, Light tuning DC and AC electrical properties of ZnO-rGO based hybrid nanocomposite film. J. Appl. Phys. **123**(9), 095115 (2018). https://doi.org/10.1063/1.5016098

5. J. Yin, F. Gao, C. Wei, Q.J.S.R. Lu, Water amount dependence on morphologies and properties of ZnO nanostructures in double-solvent system. Sci. Rep. **4**(1), 1–7 (2014). https://doi.org/10.1038/srep03736

6. M. Morsy, I. Yahia, H. Zahran, F. Meng, M.J.J.O.E.M. Ibrahim, Portable and battery operated ammonia gas sensor based on CNTs/rGO/ZnO nanocomposite. J. Electron. Mater. **48**(11), 7328–7335 (2019). https://doi.org/10.1007/s11664-019-07550-7

7. Y. Zhao, L. Liu, T. Cui, G. Tong, W.J.A.S.S. Wu, Enhanced photocatalytic properties of ZnO/reduced graphene oxide sheets (rGO) composites with controllable morphology and composition. Appl. Surf. Sci. **412**, 58–68 (2017). https://doi.org/10.1016/j.apsusc.2017.03.207

8. Y. Liu, Y. Hu, M. Zhou, H. Qian, X.J.A.C.B.E. Hu, Microwave-assisted non-aqueous route to deposit well-dispersed ZnO nanocrystals on reduced graphene oxide sheets with improved photoactivity for the decolorization of dyes under visible light. Appl. Catal. B **125**, 425–431 (2012). https://doi.org/10.1016/j.apcatb.2012.06.016

9. S.-C. Weng, S. Brahma, C.-C. Chang, J.L.J.I.J.E.S. Huang, Synthesis of self-assembled hollow-sphere ZnO/rGO nanocomposite as anode materials for lithium-ion batteries. Int. J. Electrochem. Sci **14**, 3727–3739 (2019). https://doi.org/10.20964/2019.04.63

10. Z.K. Bolaghi, S. Masoudpanah, M.J.M.R.B. Hasheminiasari, Photocatalytic activity of ZnO/RGO composite synthesized by one-pot solution combustion method. Mater. Res. Bull. **115**, 191–195 (2019). https://doi.org/10.1016/j.materresbull.2019.03.024

11. Z. Liu, L. Yu, F. Guo, S. Liu, L. Qi, M. Shan, X.J.A.S.S. Fan, Facial development of high performance room temperature NO2 gas sensors based on ZnO nanowalls decorated rGO nanosheets. Appl. Surf. Sci. **423**, 721–727 (2017). https://doi.org/10.1016/j.apsusc.2017.06.160

12. Z. Zhan, L. Zheng, Y. Pan, G. Sun, L.J.J.O.M.C. Li, Self-powered, visible-light photodetector based on thermally reduced graphene oxide–ZnO (rGO–ZnO) hybrid nanostructure. J. Mater. Chem. **22**(6), 2589–2595 (2012). https://doi.org/10.1039/C1JM13920G

13. H. Abdullah, N.A. Atiqah, A. Omar, I. Asshaari, S. Mahalingam, Z. Razali, S. Shaari, J. Mandeep, H.J.J.O.M.S.M.I.E. Misran, Structural, morphological, electrical and electron transport studies in ZnO–rGO (wt%= 0.01, 0.05 and 0.1) based dye-sensitized solar cell. J. Mater. Sci. **26**(4), 2263–2270 (2015). https://doi.org/10.1007/s10854-015-2679-y

14. K.P. Madhuri, K. Bramhaiah, N.S.J.M.R.E. John, Nanoscale photocurrent distribution in ultra-thin films of zinc oxide nanoparticles and their hybrid with reduced graphene oxide. Mater. Res. Exp. **3**(3), 035004 (2016). https://doi.org/10.1088/2053-1591/3/3/035004

15. S. Tiagulskyi, R. Yatskiv, H. Faitova, Š Kučerová, J. Vaniš, J.J.M.S.I.S.P. Grym, Electrical properties of nanoscale pn heterojunctions formed between a single ZnO nanorod and GaN substrate. Mater. Sci. Semicond **107**, 104808 (2020). https://doi.org/10.1016/j.mssp.2019.104808

16. Y. Al-Hadeethi, R.I. Badran, A. Umar, S.H. Al-Heniti, B.M. Raffah, S.J.M.E. Al-Zhrani, Electrical properties of Ga-doped ZnO nanowires/Si heterojunction diode. Mater. Exp. **10**(6), 794–801 (2020). https://doi.org/10.1166/mex.2020.1725

17. S. Nongthombam, S. Sinha, N.A. Devi, S. Rai, R. Bhujel, W.I. Singh, B.P. Swain, Charge Transfer Mechanism of Gallium Nitrite/Reduced Graphene Oxide (GaN/rGO) Nanocomposite. In: 2020 IEEE VLSI device circuit and system (VLSI DCS) 2020, pp. 171–175. IEEE. https://doi.org/10.1109/VLSIDCS47293.2020.9179877

18. M. Soylu, M.J.J.O.A. Coskun, Compounds: controlling the properties of ZnO thin films by varying precursor concentration. J. Alloys Compds. **741**, 957–968 (2018). https://doi.org/10.1016/j.jallcom.2018.01.079

19. S.K. Mandal, K. Dutta, S. Pal, S. Mandal, A. Naskar, P.K. Pal, T. Bhattacharya, A. Singha, R. Saikh, S.J.M.C. De, Physics: Engineering of ZnO/rGO nanocomposite photocatalyst towards rapid degradation of toxic dyes. Mater. Chem.

Phys. **223**, 456–465 (2019). https://doi.org/10.1016/j.matchemphys.2018.11.002

20. M. Darvishi, F. Jamali-Paghaleh, M. Jamali-Paghaleh, J.J.S. Seyed-Yazdi, Interfaces: Facile synthesis of ZnO/rGO hybrid by microwave irradiation method with improved photoactivity. Surf. Interfaces **9**, 167–172 (2017). https://doi.org/10.1016/j.surfin.2017.09.008

21. T.N. Reddy, J. Manna, R.K.J.A.A.M. Rana, interfaces: Polyamine-mediated interfacial assembly of rGO-ZnO nanostructures: a bio-inspired approach and enhanced photocatalytic properties. ACS Appl. Mater. Interfaces **7**(35), 19684–19690 (2015). https://doi.org/10.1021/acsami.5b04820

22. D.A. Reddy, R. Ma, T.K.J.C.I. Kim, Efficient photocatalytic degradation of methylene blue by heterostructured ZnO–RGO/RuO2 nanocomposite under the simulated sunlight irradiation. Ceram. Int. **41**(5), 6999–7009 (2015). https://doi.org/10.1016/j.ceramint.2015.01.155

23. M. Ghorbani, M.R. Golobostanfard, H.J.A.S.S. Abdizadeh, Flexible freestanding sandwich type ZnO/rGO/ZnO electrode for wearable supercapacitor. Appl. Surf. Sci. **419**, 277–285 (2017). https://doi.org/10.1016/j.apsusc.2017.05.060

24. P. Sengunthar, K. Bhavsar, C. Balasubramanian, U.J.A.P.A. Joshi, Physical properties and enhanced photocatalytic activity of ZnO-rGO nanocomposites. Appl. Phys. A **126**(7), 1–9 (2020). https://doi.org/10.1007/s00339-020-03753-6

25. D.C. Marcano, D.V. Kosynkin, J.M. Berlin, A. Sinitskii, Z. Sun, A. Slesarev, L.B. Alemany, W. Lu, J.M.J.A.N. Tour, Improved synthesis of graphene oxide. ACS Nano **4**(8), 4806–4814 (2010). https://doi.org/10.1021/nn1006368

26. O.J.C. Akhavan, The effect of heat treatment on formation of graphene thin films from graphene oxide nanosheets. Carbon **48**(2), 509–519 (2010). https://doi.org/10.1016/j.carbon.2009.09.069

27. R. Bomila, A. Venkatesan, S.J.O. Srinivasan, Structural, luminescence and photocatalytic properties of pure and octylamine capped ZnO nanoparticles. Optik **158**, 565–573 (2018). https://doi.org/10.1016/j.ijleo.2017.12.141

28. H.-H. Huang, K.K.H. De Silva, G. Kumara, M.J.S.R. Yoshimura, Structural evolution of hydrothermally derived reduced graphene oxide. Sci. Rep. **8**(1), 1–9 (2018). https://doi.org/10.1038/s41598-018-25194-1

29. J. Jayachandiran, J. Yesuraj, M. Arivanandhan, A. Raja, S.A. Suthanthiraraj, R. Jayavel, D.J.J.O.I. Nedumaran, O. Polymers, Materials: Synthesis and electrochemical studies of rGO/ZnO nanocomposite for supercapacitor application. J. Inorg. Organometall. Polym. Mater. **28**(5), 2046–2055 (2018). https://doi.org/10.1007/s10904-018-0873-0

30. G. Qu, G. Fan, M. Zhou, X. Rong, T. Li, R. Zhang, J. Sun, D.J.A.O. Chen, Graphene-modified ZnO nanostructures for low-temperature NO2 sensing. ACS Omeg **4**(2), 4221–4232 (2019). https://doi.org/10.1021/acsomega.8b03624

31. K. Ravi, B.S. Mohan, G.S. Sree, I.M. Raju, K. Basavaiah, B.V.J.I.J.C.S. Rao, ZnO/RGO nanocomposite via hydrothermal route for photocatalytic degradation of dyes in presence of visible light. Int J Chem Stud **6**(6), 20–26 (2018)

32. K. Arora, S. Srivastava, P.R. Solanki, N.K.J.I.S.J. Puri, Electrochemical hydrogen gas sensing employing palladium oxide/reduced graphene oxide (PdO-rGO) nanocomposites. IEEE Sens. J. **19**(18), 8262–8271 (2019). https://doi.org/10.1109/JSEN.2019.2918360

33. B.D. Cullity, *Elements of X-ray Diffraction* (Addison-Wesley Publishing, Boston, 1956)

34. A. Goktas, A. Tumbul, Z. Aba, M.J.T.S.F. Durgun, Mg doping levels and annealing temperature induced structural, optical and electrical properties of highly c-axis oriented ZnO: Mg thin films and Al/ZnO: Mg/p-Si/Al heterojunction diode. Thin Solid Films **680**, 20–30 (2019)

35. A. Tumbul, F. Aslan, S. Demirozu, A. Goktas, A. Kilic, M. Durgun, M.Z.J.M.R.E. Zarbali, Solution processed boron doped ZnO thin films: influence of different boron complexes. Mater. Res. Exp. **6**(3), 035903 (2018). https://doi.org/10.1088/2053-1591/aaf4d8

36. H. Mohseni, H. Shokrollahi, I. Sharifi, K.J.J.O.M. Gheisari, M. Materials, Magnetic and structural studies of the Mn-doped Mg–Zn ferrite nanoparticles synthesized by the glycine nitrate process. J. Magn. Magn. Mater. **324**(22), 3741–3747 (2012)

37. D. Bobade, S. Rathod, M.L.J.P.B.C.M. Mane, Sol–gel auto-combustion synthesis, structural and enhanced magnetic properties of Ni2+ substituted nanocrystalline Mg–Zn spinel ferrite. Physica B **407**(18), 3700–3704 (2012). https://doi.org/10.1016/j.physb.2012.05.017

38. P. Labhane, L. Patle, V. Huse, G. Sonawane, S.J.C.P.L. Sonawane, Synthesis of reduced graphene oxide sheets decorated by zinc oxide nanoparticles: crystallographic, optical, morphological and photocatalytic study. Chem. Phys. Lett. **661**, 13–19 (2016). https://doi.org/10.1016/j.cplett.2016.08.041

39. A. Goktas, F. Aslan, I.H.J.J.O.M.S.M.I.E. Mutlu, Annealing effect on the characteristics of La 0.67 Sr 0.33 MnO3 polycrystalline thin films produced by the sol–gel dip-coating process. J. Mater. Sci. **23**(2), 605–611 (2012)

40. A. Goktas, F. Aslan, B. Yeşilata, I.J.M.S.I.S.P. Boz, Physical properties of solution processable n-type Fe and Al co-doped ZnO nanostructured thin films: role of Al doping levels and annealing. Mater. Sci. Semicond. Process. **75**, 221–233 (2018). https://doi.org/10.1016/j.mssp.2017.11.033

41. Y.-L. Chen, Z.-A. Hu, Y.-Q. Chang, H.-W. Wang, Z.-Y. Zhang, Y.-Y. Yang, Wu, H.-Y.J.T.J.o.P.C.C., Zinc oxide/

reduced graphene oxide composites and electrochemical capacitance enhanced by homogeneous incorporation of reduced graphene oxide sheets in zinc oxide matrix. J. Phys. Chem. C **115**(5), 2563–2571 (2011). https://doi.org/10.1021/jp109597n

42. A. Göktaş, A. Tumbul, F.J.J.O.S.-G.S. Aslan, Technology: Grain size-induced structural, magnetic and magnetoresistance properties of Nd 0.67 Ca 0.33 MnO3 nanocrystalline thin films. J Sol-Gel Sci Technol **78**(2), 262–269 (2016)

43. S. Dewan, M. Tomar, R. Tandon, V.J.J.O.A.P. Gupta, Zn doping induced conductivity transformation in NiO films for realization of pn homo junction diode. J. Appl. Phys. **121**(21), 215307 (2017). https://doi.org/10.1063/1.4984580

44. X. Liu, L. Pan, Q. Zhao, T. Lv, G. Zhu, T. Chen, T. Lu, Z. Sun, C.J.C.E.J. Sun, UV-assisted photocatalytic synthesis of ZnO–reduced graphene oxide composites with enhanced photocatalytic activity in reduction of Cr (VI). Chem. Eng. J. **183**, 238–243 (2012). https://doi.org/10.1016/j.cej.2011.12.068

45. B. Li, H.J.J.O.M.C. Cao, ZnO@ graphene composite with enhanced performance for the removal of dye from water. J. Mater. Chem. **21**(10), 3346–3349 (2011). https://doi.org/10.1039/C0JM03253K

46. L. Shi, S.J.N.R.I. Gunasekaran, Preparation of pectin–ZnO nanocomposite. Nanoscale Res. Lett. **3**(12), 491–495 (2008). https://doi.org/10.1007/s11671-008-9185-6

47. N. Bano, I. Hussain, A. El-Naggar, A.J.A.P.A. Albassam, Reduced graphene oxide nanocomposites for optoelectronics applications. Appl. Phys. **125**(3), 1–7 (2019). https://doi.org/10.1007/s00339-019-2518-8

48. M.E. Uddin, R.K. Layek, N.H. Kim, D. Hui, J.H.J.C.P.B.E. Lee, Preparation and properties of reduced graphene oxide/polyacrylonitrile nanocomposites using polyvinyl phenol. Compos. B **80**, 238–245 (2015). https://doi.org/10.1016/j.compositesb.2015.06.009

49. S. Kumar, V. Pandit, K. Bhattacharyya, V.J.M.C. Krishnan, Physics: Sunlight driven photocatalytic reduction of 4-nitrophenol on Pt decorated ZnO-RGO nanoheterostructures. Mater. Chem. Phys. A **214**, 364–376 (2018). https://doi.org/10.1016/j.matchemphys.2018.04.113

50. C. Rodwihok, D. Wongratanaphisan, Y.L. Thi Ngo, M. Khandelwal, S.H. Hur, J.S.J.N. Chung, Effect of GO additive in ZnO/rGO nanocomposites with enhanced photosensitivity and photocatalytic activity. Nanomaterials **9**(10), 1441 (2019). https://doi.org/10.3390/nano9101441

51. R. Beura, P.J.J.O.P. Thangadurai, C.O. Solids, Structural, optical and photocatalytic properties of graphene-ZnO nanocomposites for varied compositions. J. Phys. Chem. Solids **102**, 168–177 (2017). https://doi.org/10.1016/j.jpcs.2016.11.024

52. H. Fan, X. Zhao, J. Yang, X. Shan, L. Yang, Y. Zhang, X. Li, M.J.C.C. Gao, ZnO–graphene composite for photocatalytic degradation of methylene blue dye. Catal. Commun. **29**, 29–34 (2012). https://doi.org/10.1016/j.catcom.2012.09.013

53. Y.T. Li, J.M. Xu, Z.J. Tang, T.T. Xu, X.J.J.J.O.A. Li, Compounds: Nearly white light photoluminescence from ZnO/rGO nanocomposite prepared by a one-step hydrothermal method. J. Alloys Compds. **715**, 122–128 (2017). https://doi.org/10.1016/j.jallcom.2017.04.286

54. X. Díez-Betriu, S. Álvarez-García, C. Botas, P. Álvarez, J. Sánchez-Marcos, C. Prieto, R. Menéndez, A.J.J.O.M.C.C. De Andrés, Raman spectroscopy for the study of reduction mechanisms and optimization of conductivity in graphene oxide thin films. J. Mater. Chem. C **1**(41), 6905–6912 (2013)

55. H. Liu, M. Xiang, X.J.J.O.M.S. Shao, Graphene/ZnO nanocomposite with seamless interface renders photoluminescence quenching and photocatalytic activity enhancement. J. Mater. Sci. **53**(19), 13924–13935 (2018). https://doi.org/10.1007/s10853-018-2605-9

56. S. Demirezen, A. Kaya, Ö. Vural, Ş.J.M.S.I.S.P. Altındal, The effect of Mo-doped PVC+ TCNQ interfacial layer on the electrical properties of Au/PVC+ TCNQ/p-Si structures at room temperature. Mater. Sci. Semicond. Process **33**, 140–148 (2015). https://doi.org/10.1016/j.mssp.2015.01.050

57. S.A. Yerişkin, M. Balbaşı, I.J.J.O.M.S.M.I.E. Orak, The effects of (graphene doped-PVA) interlayer on the determinative electrical parameters of the Au/n-Si (MS) structures at room temperature. J. Mater. Sci. Mater. Electron. **28**(18), 14040–14048 (2017). https://doi.org/10.1007/s10854-017-7255-1

58. S. Safa, R. Sarraf-Mamoori, R. Azimirad, The effects of reduced graphene oxide (rGO) on ZnO film UV-detector. In: Advanced Materials Research 2014, pp. 577–582. Trans Tech Publ. https://doi.org/10.4028/www.scientific.net/AMR.829.577

59. A. Eroğlu, S. Demirezen, Y. Azizian-Kalandaragh, S.S.J.J.O.M.S.M.I.E. Altındal, A comparative study on the electrical properties and conduction mechanisms of Au/n-Si Schottky diodes with/without an organic interlayer. J. Mater. Sci **31**(17), 14466–14477 (2020). https://doi.org/10.1007/s10854-020-04006-1

60. M. Mohiuddin, B. Kumar, S.J.B.C.I.E. Haque, Biopolymer composites in photovoltaics and photodetectors. Biopolym. Compos. Electron. **45**, 459–486 (2017). https://doi.org/10.1016/B978-0-12-809261-3.00017-6

61. B. Murali, S.J.D.T. Krupanidhi, Transport properties of CuIn 1–x Al x Se 2/AZnO heterostructure for low cost thin film photovoltaics. Dalton Trans. **43**(5), 1974–1983 (2014). https://doi.org/10.1039/C3DT52515E

62. X. Yan, H. Hao, Y. Chen, S. Shi, E. Zhang, J. Lou, Liu, B.J.N.R.l., Self-rectifying performance in the sandwiched structure of Ag/In-Ga-Zn-O/Pt bipolar resistive switching memory. Nanoscale Res. Lett. **9**(1), 1–6 (2014). https://doi.org/10.1186/1556-276X-9-548

63. E. Tanrıkulu, S. Demirezen, Ş Altındal, İJ.J.O.M.S.M.I.E. Uslu, Analysis of electrical characteristics and conduction mechanisms in the Al/(% 7 Zn-doped PVA)/p-Si (MPS) structure at room temperature. J Mater Sci **28**(12), 8844–8856 (2017). https://doi.org/10.1007/s10854-017-6613-3

64. S. Demirezen, S.A.J.P.B. Yerişkin, A detailed comparative study on electrical and photovoltaic characteristics of Al/p-Si photodiodes with coumarin-doped PVA interfacial layer: the effect of doping concentration. Polym. Bull. **77**(1), 49–71 (2020). https://doi.org/10.1007/s00289-019-02704-3

65. S. Demirezen, H. Çetinkaya, M. Kara, F. Yakuphanoğlu, ŞJ.S. Altındal, A.A. Physical, Synthesis, electrical and photo-sensing characteristics of the Al/(PCBM/NiO: ZnO)/p-Si nanocomposite structures. Sens. Actuators A **317**, 112449 (2021). https://doi.org/10.1016/j.sna.2020.112449

66. Chiu, F.-C., Pan, T.-M., Kundu, T.K., Shih, C.-H.: Thin film applications in advanced electron devices. In. Hindawi, (2014). https://doi.org/10.1155/2014/927358